The Astrophysical Journal Letters, 923:L20 (11pp), 2021 December 10 https://doi.org/10.3847/2041-8213/ac3ec8

Chemically Fresh Gas Inflows Detected in a Nearby High-mass Star-forming Region

Xi Chen[1,2], Zhi-Yuan Ren[3], Da-Lei Li[4], Tie Liu[2], Ke Wang[5], Zhi-Qiang Shen[2], Simon P. Ellingsen[6], Andrej M. Sobolev[7], Ying Mei[1], Jing-Jing Li[8], Yue-Fang Wu[5], and Kee-Tae Kim[9,10]
[1] Center for Astrophysics, Guangzhou University, Guangzhou 510006, People's Republic of China; chenxi@gzhu.edu.cn
[2] Shanghai Astronomical Observatory, Chinese Academy of Sciences, 80 Nandan Road, Shanghai 200030, People's Republic of China
[3] National Astronomical Observatories, Chinese Academy of Sciences, Datun Rd. A20, Beijing, People's Republic of China; renzy@nao.cas.cn
[4] Xinjiang Astronomical Observatory, Chinese Academy of Sciences, 830011 Urumqi, People's Republic of China
[5] Kavli Institute for Astronomy and Astrophysics, Peking University, 5 Yiheyuan Road, Haidian District, Beijing 100871, People's Republic of China
[6] School of Natural Sciences, University of Tasmania, Private Bag 37, Hobart, Tasmania 7001, Australia
[7] Ural Federal University, 19 Mira Street, 620002 Ekaterinburg, Russia
[8] Purple Mountain Observatory, Chinese Academy of Sciences, Nanjing 210008, People's Republic of China
[9] Korea Astronomy and Space Science Institute, 776 Daedeokdae-ro, Yuseong-gu, Daejeon 34055, Republic Of Korea
[10] University of Science and Technology, Korea (UST), 217 Gajeong-ro, Yuseong-gu, Daejeon 34113, Republic Of Korea
Received 2021 August 24; revised 2021 November 30; accepted 2021 November 30; published 2021 December 14

Abstract

We report the detection of a chemically fresh inflow that is feeding high-mass young-stellar-object (HMYSO) growth in the nearby high-mass star-forming region G352.63 made with both the Atacama Large Millimeter/submillimeter Array (ALMA) and the Submillimeter Array (SMA). High-quality images of the dust and molecular lines from both ALMA and SMA have consistently revealed a gravitationally controlled cold (∼10 K) gas inflow of chemically fresh molecules (e.g., CCH and HC_3N) toward the central HMYSO and its surrounding dense gas structure, which has a possible torus- or disk-like morphology. The HMYSO is also observed to have an outflow, which is nearly perpendicular to the torus and its parental filament, and thus can be clearly separated from the inflows. These kinematic features provide observational evidence to support the conjecture that the infalling streamers in high-mass star-forming regions could proceed in a similar process to that observed in low-mass counterparts. The chemically fresh infalling streamers could also be involved in the disk or torus configuration, fragmentation, and accretion bursts that occur in both simulations and observations.

Unified Astronomy Thesaurus concepts: Star formation (1569); Young stellar objects (1834); Interstellar clouds (834); Interstellar medium (847); Protostars (1302); Stellar accretion disks (1579)

Compared with the detailed framework of the low-mass star formation, a generally accepted scheme for the high-mass counterparts (with mass $>8\,M_{\odot}$) is still not fully established (Zinnecker & Yorke 2007; Tan et al. 2014). The basic components (i.e., disks, outflows and filaments) of the low-mass star formation picture created by Shu et al. (1987) have been long observed toward a number of sources thanks in part to the fact that many low-mass protostars are located within 500 pc of Earth. Several representative models are proposed to explain the process of high-mass ones, including the collapse of a single massive core (e.g., McKee & Tan 2002, 2003) or competitive accretion (e.g., Bonnell et al. 2004; Bonnell & Bate 2006). Thanks to recent high-resolution interferometers including the Submillimeter Array (SMA) and Atacama Large Millimeter/submillimeter Array (ALMA), very detailed physical and kinematic properties have been detected toward high-mass young stellar objects (HMYSOs) such as disks (Johnston et al. 2015; Ilee et al. 2016; Zapata et al. 2019), outflows (Goddi et al. 2020; Zinchenko et al. 2020), and filamentary structures (Chen et al. 2019a; Hacar et al. 2018). This suggests that the HMYSOs could have traits comparable to those of low-mass YSOs in terms of their spatial morphologies and accretion mechanisms.

Hydrodynamical simulations further predicted asymmetric accretion streamers to be an important ingredient for mass accretion in both low- and high-mass star formation (Kuffmeier et al. 2019; Kuznetsova et al. 2019; Wurster et al. 2019). These models have obtained concrete support from increasing number of streamers and filamentary inflows observed in low- and intermediate-mass YSOs (e.g., Pineda et al. 2020; Murillo et al. 2021; Ren et al. 2021; Thieme et al. 2021). The observed inflows often have mass infall rates comparable to the disk accretion or core collapse. And the inflows are observed in chemically fresh molecules with compact and collimated morphologies toward the central YSOs, which suggest their capability of directly transferring the ambient dense gas into accretion.

In this sense, it becomes more interesting to explore the asymmetric accretion inflows in high-mass star formation. Actually, many prominent inflows or even global collapse massive filaments have been detected (e.g., Peretto et al. 2013; Tackenberg et al. 2014; Yuan et al. 2018; Chen et al. 2020a; Yuan et al. 2020; Hu et al. 2021; Avison et al. 2021; Sanhueza et al. 2021). But their connection to individual HMYSOs has not yet been confirmed. This is mainly due to the frequently clustered environments and larger distances of the HMYSOs compared to low-mass ones (Zinnecker & Yorke 2007 and references therein; Tobin et al. 2016). Better resolved sources are expected to help us evaluate the detailed properties of the massive inflows and enable comparison with other formation theories. In this contribution, one should look for more isolated HMYSOs at smaller distances (<1 kpc). High-angular-resolution interferometry (e.g., ALMA) observations are also indispensable for revealing spatial structures. G352.63–1.07

(G352.63 hereafter) is a high-mass star-forming region associated with 6.7 GHz methanol masers. Trigonometric parallax of the masers measured a distance of 0.69 kpc, which locates it in an interarm region (Chen et al. 2019b) wherein the gas environment could be much less clustered than the Galactic-arm regions. It could thus be an ideal target for investigating the accretion process in HMYSO. In this Letter, we report that a bipolar outflow, gravitationally controlled, infalling gas flow and rotational disk (or torus) structure is associated with the HMYSO in this region detected with ALMA and SMA.

1. Observation and Data Reduction

1.1. ALMA Observations

G352.63 is one of the target regions in the ATOMS ("ALMA Three-millimeter Observations of Massive Star-forming regions") survey (Project ID: 2019.1.00685.S; Liu et al. 2020). The survey sample consists of 146 dense gas clumps selected from IRAS point sources. G352.63 has source ID 101 in the ATOMS sample and the ALMA observations were made on 2019 December 19. For this source, the observations consist of a single pointing with both the Atacama Compact 7 m Array (ACA; Morita Array) and the 12 m array (C43-2 or C43-3 configurations) in ALMA band 3. The eight spectral windows (SPWs) were tuned to cover 11 commonly observed molecular lines in this frequency range, including those we have focused on in this work (CCH $1-0$, 87.317 GHz; HCO^+ $1-0$, 89.189 GHz and HC_3N 11−10, 100.076 GHz).

The SPWs covering the CCH and HCO^+ lines have a velocity resolution of ∼0.2 km s^{-1}, while those covering the HC_3N lines have a lower velocity resolution of ∼1.4 km s^{-1}. Calibration and imaging were carried out using the CASA software package version 5.6 and for the array configuration we are able to image spatial structures with angular scales of up to ∼20″ in radius. More details about data reduction can be found in Liu et al. (2020). The typical synthesized beam for the reduced combined ACA+12 m array data images is $2\farcs5 \times 2\farcs1$ (P.A. = 88°) for the CCH and HCO^+ lines, and is $2\farcs2 \times 1\farcs8$ (P.A. = 88°) for the HC_3N lines. The rms noise of the images is better than 10 mJy $beam^{-1}$ per channel.

1.2. SMA Observations

The SMA observations toward G352.63 were made on 2017 August 3, with the array in its compact configuration. The SWARM correlator was used in dual receiver mode with an 8 GHz bandwidth per sideband. The 230 GHz and 240 GHz receivers were used to cover the main targeted lines in this work, which included ^{12}CO (2–1; 230.538 GHz), HCO^+ (3–2; 267.557 GHz), DCN (3-2; 217.238 GHz), DCO^+ (4-3; 288.143 GHz), and a series of CH_3CN (12–11; ∼220 GHz) and H_2CO (3–2; ∼218 GHz) lines. The spectral channel width was about 0.5 MHz, corresponding to a velocity resolution of ∼0.7 km s^{-1} at 230 GHz, and ∼0.5 km s^{-1} at 280 GHz. The time-dependent antenna gains were calibrated using regular observations of the quasar 1700–261. The bandpass response was calibrated by observing the quasar 3C454.3 and the absolute flux density was determined from observations of Neptune and Titan.

The visibility data were calibrated using the IDL superset MIR. The imaging and analysis were undertaken in MIRIAD. The synthesized beam size, i.e., the angular resolution of the image data, is approximately $5\farcs8 \times 2\farcs4$ at 230 GHz and $4\farcs7 \times 1\farcs9$ at 285 GHz, with a position angle of −12.°3 northwest. The typical rms noise is ∼50 mJy $beam^{-1}$ in a spectral channel for the molecular line data. We used the line-free channels in the frequency range 281–289 GHz to produce the 1.1 mm dust emission image. The rms noise for the dust emission image is ∼4 mJy $beam^{-1}$.

2. Results and Discussions

2.1. Bipolar Outflow

Figure 1(a) is the Herschel/SPIRE 250 μm continuum image. It exhibits two dense clumps, wherein the northern clump is the target for this work. It has a roughly spherical shape, with an average diameter of ∼45″. It can be well separated from the southern gas clump despite weak gas connection. We measured its peak flux density in each Herschel band to model the spectral energy distribution (SED) as shown in Figure 1(b). Using the graybody emission model, we can closely fit the SED with a single temperature component of $T_{\rm dust} = 25$ K. This suggests that the clump should have a unified cold dense state and does not have very strong internal stellar heating.

Figure 1(c) shows the ALMA 3 mm and SMA 1.1 mm dust continuum emissions. The two image data sets have a spatial resolution of ∼0.01 pc and should closely trace the dense-core gas. Their contours are overlaid on the 2MASS 2 μm Ks image. Five dust condensations can be clearly identified, labeled as M1 to M5. M1 is the most compact one, also associated with strong 6.7 GHz methanol maser emission (Chen et al. 2019b), which is so far considered to be an exclusive indicator for HMYSO (Xu et al. 2008).

The 2MASS 2μm image (Figure 1(c)) exhibits an intense bipolar emission feature with a roughly symmetrical distribution over M1. The intense 2MASS 2 μm emission usually traces the shock-excited molecular H_2 emission. It suggests the presence of strong outflow activities around M1, which may have a morphology comparable to the shocked outflow in IRAS 20126+4104 (Cesaroni et al. 2013).

We inspected the molecular outflow from the ALMA HCO^+ (1–0) emission. It indeed shows noticeable high-velocity line wings with considerable intensities, as shown in Figure 1(d). The line wings (inset panel) extend to $v_{\rm LOS} = \pm 20$ km s^{-1} on the blue and redshift sides, respectively. The integration emission of the line wings is plotted in contours and overlaid on the Spitzer/IRDC color-composed three-band image. One can see that the IRAC 4.5 μm emission (green extended emission) shows a large overlapped spatial extent with the HCO^+ outflow emissions. The outflow morphology also largely overlaps with the 2MASS emission in Figure 1(c). The outflow components have a symmetric distribution with respect to M1. In contrast to the outflow and shock emissions, the dense and warm gas tracers (e.g., CH_3CN and CH_3OH transitions) are only detected toward M1. The CH_3CN transitions provide a gas temperature estimate of ∼170 K (see Appendix A). M1 thus should be a compact hot molecular core driving the bipolar outflow.

The bipolar outflow has a large opening angle of ∼60°, as denoted by the dashed lines in Figure 1(d). Considering its spatial extent of 2×10^4 au (or 0.1 pc) from the driving source, and assuming an inclination angle of 60° with respect to the line of sight (LOS; same as the angle of inclination of the

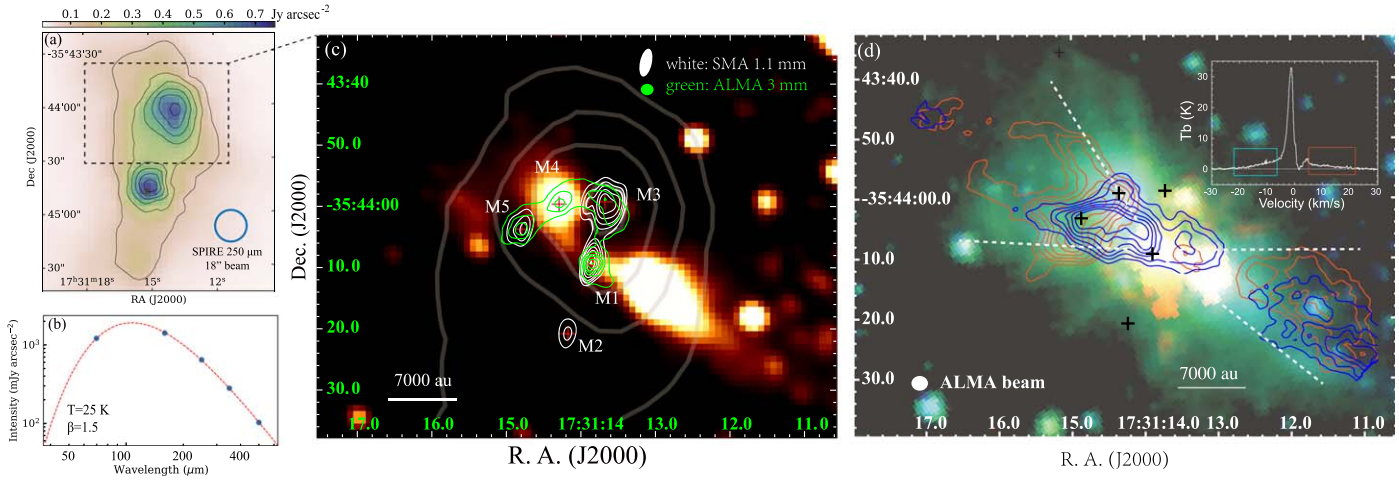

Figure 1. (a) Herschel/SPIRE 250 μm continuum image over the parental clump of G352.63. The intensity is scaled to units of Jy arcsec^{-1}. The contour levels are 40% to 90% of the peak intensity in step of 10%. (b) The spectral energy distribution (SED) of the parental clump. The intensity at each band represents the value that is scaled to the 500 μm resolution (36″ beam, in units of Jy arcsec^{-1}). (c) The millimeter continuum emissions observed with ALMA and SMA. Green contours: the 3 mm dust emission detected with ALMA, with contour levels of 0.1, 0.2, 0.3, 0.4, 0.6, and 0.8 times the peak value (10 mJy beam^{-1}). White contours: 1.1 mm dust emission detected with SMA, with contour levels of 3, 5, 7, 10, 13, 16, and 19 times 4 mJy beam^{-1} (rms level). The corresponding dust emission components are marked as M1–M5. The beam shapes are plotted with ellipses. The background is the near-infrared 2MASS Ks 2 μm image. (d) Contours: the HCO$^+$ ($J = 1 - 0$) outflow detected with ALMA. The blue and red contours represent the integrated emission in the velocity ranges of (-22, -5) and (5, 22) km s^{-1}, respectively. The contour levels are 3, 5, 7, 9, 11, and 13 times the rms level (0.1 Jy beam^{-1} km s^{-1}). The background image is the color-composed GLIMPSE IRAC image of 8.0 μm (red), 4.5 μm (green), and 3.6 μm (blue) bands.

disk/torus rotational axis; see Section 2.2), it then implies a dynamic ages of ∼3600 yr.

2.2. Velocity Profile: Torus around the HMYSO

Figure 2(a) shows the integrated emission regions of the DCN, DCO$^+$, and H_2CO observed with the SMA. It shows that together their emission regions are aligned in the same direction along M1, M2, and M3 at a position angle of +15° to the northwest. The DCN and H_2CO emission regions are largely overlapped, both extending from M2 to M3, and peak around M1. In comparison, the DCO$^+$ exhibits two discrete emission features overlaid with M2 and M3, respectively.

In order to inspect the gas motion of the three condensations, we plot the position–velocity (P–V) diagram along the M2–M1–M3 direction, as shown in Figures 2(b) and (c). The noticeable feature is that both DCN and H_2CO exhibit a continuous velocity increase toward the center of M1. The blueshifted side reaches the peak velocity almost directly at M1, while the redshifted side also tends to have a less prominent but roughly symmetric increasing trend toward center, as labeled with the dashed curves. Such a velocity distribution is comparable to other Keplerian-rotating disks (e.g., Beltrán et al. 2014). It suggests that M1 and its surrounding gas could have a quasi-Keplerian rotation. By fitting the velocity profile using a Keplerian mode (dashed lines, see Appendix B), we can estimate the dynamical mass of the central star to be $M_* = 9.0/\sin^2\theta\, M_\odot$, where θ is the inclination angle of the rotational disk plane relative to the sky plane. It is likely that the disk/torus is mainly traced by the H_2CO and DCN, while the two DCO$^+$ condensations (i.e., M2 and M3) are located at the edges. Overall spatial extent is indicated by the dashed ellipse in Figure 2(a).

The disk-like structure is also supported by the symmetric DCO$^+$ emissions on the two sides of M1. DCO$^+$ was found to trace the coldest disk locations (Pety et al. 2007; Ginard et al. 2012) and the outer disk ring in a protostar (Öberg et al. 2015). In G352.63, the two DCO$^+$ components close to M2 and M3 could reflect higher material accumulation at those locations due to an edge-brightening effect along the LOS or perhaps a thickened outer ring at the edge (similar to a "doughnut").

The H_2CO and DCN emission regions have a length of 1.4×10^4 au, which could represent the upper limit for the spatial extent of the rotating structure, i.e., $r \sim 10''$ or 7000 au. This value is larger than the typical size of $r \sim 1000$ au for other HMYSO disks revealed in ALMA observations (e.g., Johnston et al. 2015; Ilee et al. 2016; Zapata et al. 2019; Goddi et al. 2020; Maud et al. 2018, 2019). Compared to those typical compact disks, G352.63 could have a more extended torus structure around M1, with more irregular-shaped, complicated, internal mass distribution with a large fraction of mass residing near the edges. It could be more similar to the circumstellar disk/torus with comparable radius (8000–12,000 au) that was detected around the clump SMA1 in S255N (Zemlyanukha et al. 2018). Moreover, the torus around M2–M1–M3 could already have a possible fragmentation. However, due to overall elongation perpendicular to the outflow direction as well as the roughly continuous increasing velocity trend toward M1 (Figures 2(b) and (c)), the torus could still be maintained as gravitational bounded structure around M1. Meanwhile, M1 is possible to have an inner disk immediately around the central star within radius of $<1''$ (or <700 au) so as to explain the quasi-Keplerian velocity-increasing feature therein. It calls for higher resolution and more optically thin tracers in future studies to probe the inner disk.

2.3. Chemically Fresh Gas Inflows

We inspected the dense gas distribution from the molecular tracers observed with ALMA. The peak emission and peak velocity maps of the two dense gas tracers, HC_3N and CCH, are shown in Figures 3(a) and (b), respectively. The two species exhibit an overall north–south oriented filament with a scale of ∼30″ (0.1 pc). The filament directly covers the direction from M2 to M3, and extends further to the north and south. Compared to the spatial layout of the torus, one can

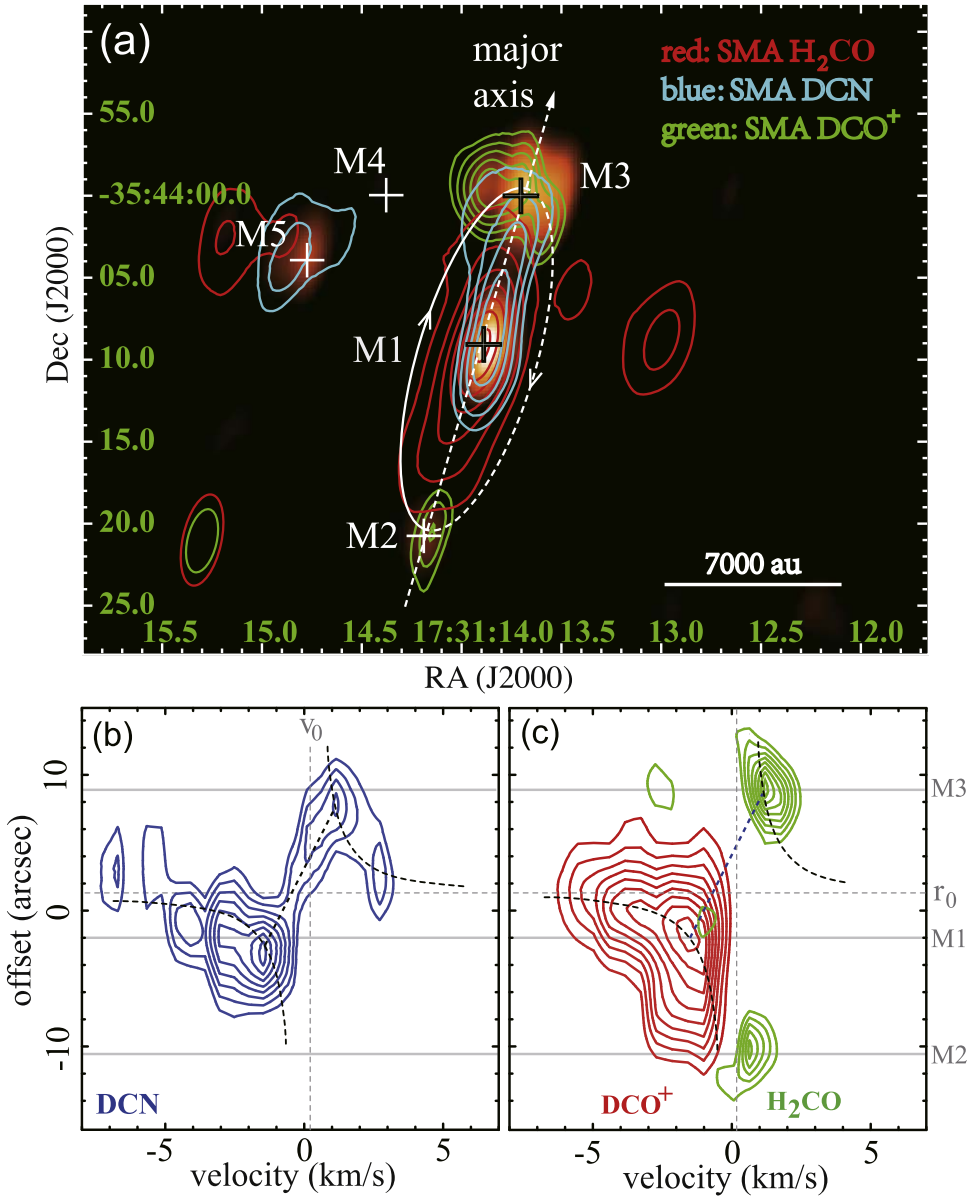

Figure 2. The emission regions and velocity distributions of the dense gas around M1 detected with SMA. (a) The integrated emissions of H_2CO 3(0,3)–2(0,2) 218.222 GHz (red contours), DCN 3–2 217.238 GHz (blue contours), and DCO^+ 4–3 288.143 GHz (green contours). The contour levels are: (3, 4, 6, 8, 10) × 0.5 Jy beam^{-1} km s^{-1} for HCO^+, (3, 4, 5, 6, 7) × 0.5 Jy beam^{-1} km s^{-1} for DCN, and (3, 4, 5, 6, 7) × 0.15 Jy beam^{-1} km s^{-1} for DCO^+. The background is the 1.1 mm dust continuum observed with SMA. The beam shapes at 230 GHz and 280 GHz bands are shown in the bottom left with red and green ellipses, respectively. The white dashed ellipse represents the expected torus region as suggested by the three molecules and dust emission. The solid half-ellipse denotes the eastern side of the torus inclined toward the observer. The dashed arrow denotes the elongated direction of the gas structure, which could be the possible midplane of the torus. (b) and (c) Position–velocity (P–V) diagrams of the three species along the major axis. The origin of each P–V diagram is at the 1.1 mm continuum peak. The contour levels of the P–V diagrams start from 30% in steps of 10% of their peaks (1.98 Jy beam^{-1} for H_2CO, 0.74 Jy beam^{-1} for DCN, and 0.88 Jy beam^{-1} DCO^+). The best Kepler rotation model is shown in the dashed curves and described in Appendix B.

see that the torus is formed in parallel with the parental filament, while the rotating axis and bipolar outflow are perpendicular to the filament.

We also note that the two species are both chemically early-type molecules (Bergin & Tafalla 2007; Pineda et al. 2020), thus are expected to trace colder gas regions. The gas temperature of two CCH hyperfine transitions derived from our observations is typically ∼10 K (using Equations (C1) and (C2) in Appendix C), which is consistent with that measured by others (Ginard et al. 2012; Sanhueza et al. 2013). These species are likely to be disrupted in more evolved dense cores, causing the HC_3N and CCH emissions to deviate from the dust continuum.

These two chemically early-type species both exhibit active kinematical features. As shown in Figures 3(a) and (b) along the filament, the peak velocity maps show blueshifted velocities from M2 to M1 and redshifted velocities from M1 to M5 at a scale of $v - v_{sys} = 1.5$ to 2 km s^{-1}, suggesting prominent gas interactions at the torus edges. In order to further investigate the gas motion, we plot the velocity dispersion map of CCH as shown in Figure 3(c). It exhibits three major increasing features, labeled as area 1, 2, and 3. Area 1 is

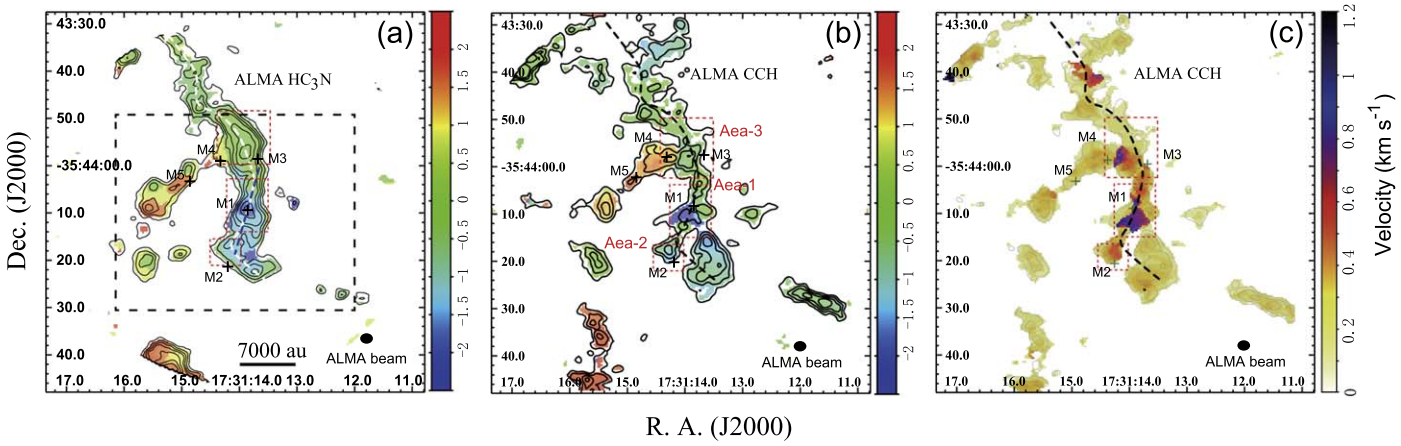

Figure 3. Infalling streamers of chemically fresh molecules detected toward the targeted region. (a) The peak emission region (contours) overlaid on the peak velocity (false-color background) for the HC_3N $J = 11 - 10$ transition. The contour levels are (3, 4, 5, 6, 8, 10, 12) × 0.015 Jy beam^{-1}. The black dashed box defines the zoomed view field of two infalling streamers shown in Figures 4 and 5. The dashed curve denotes the ridge line of the major filament. (b) Same as (a) but for the CCH transition with contour levels of (3, 4, 5, 6) × 0.03 Jy beam^{-1}. (c) Velocity dispersion of the CCH line. The three areas with significant increasing velocity dispersion features are denoted as Area 1, 2, and 3 with red dashed boxes, respectively.

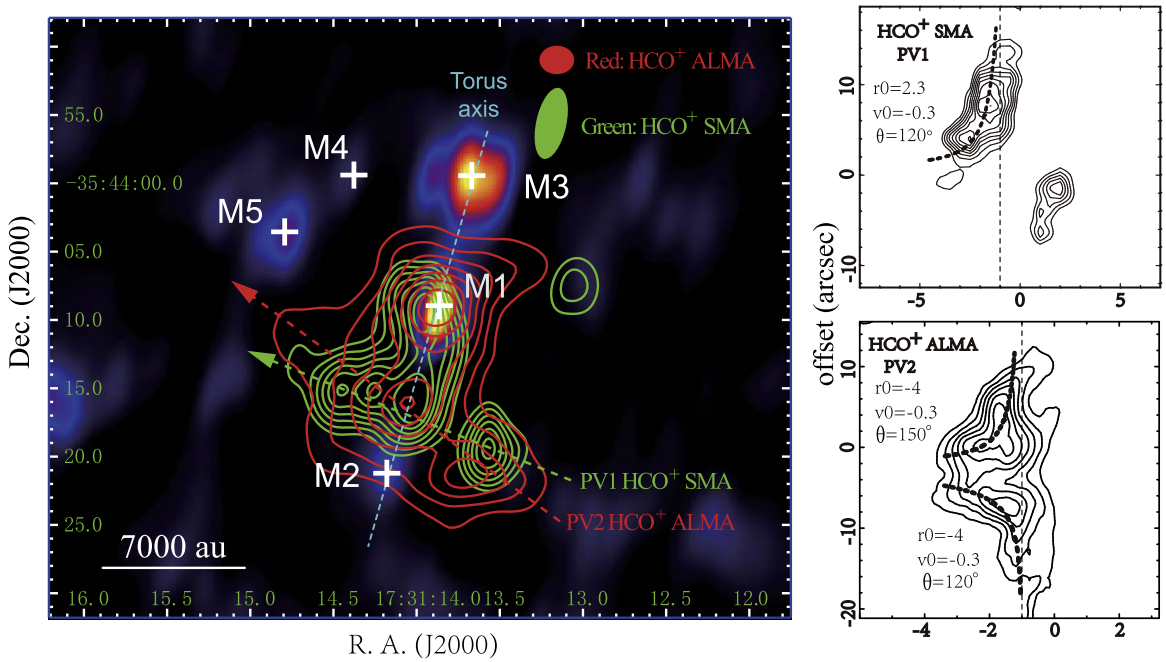

Figure 4. The gravitationally controlled southeastern infalling streamer (Streamer 1) traced by the integrated line emission from the HCO$^+$ transitions. The red contours shows the HCO$^+$ (1–0) observed with ALMA, with contours levels starting from 3 Jy beam^{-1} km s^{-1} in steps of 1 Jy beam^{-1} km s^{-1}. The green contours shows the HCO$^+$ (3–2) observed with SMA, with levels starting from 0.9 Jy beam^{-1} km s^{-1} in steps of 0.3 Jy beam^{-1} km s^{-1}. The beam shapes of the two observations are shown with ellipses. The background image is the 1.1 mm dust emission detected with SMA. The right subpanels show the P–V diagrams along Streamer 1 as labeled with dashed lines (the HCO$^+$ (2–1) and (1–0) emissions have slightly different ridge lines). The contour levels of the P–V diagrams start from 30% in steps of 10% of the peak value (5.36 Jy beam^{-1} for the SMA HCO$^+$; 0.89 Jy beam^{-1} for the ALMA HCO$^+$). The best freefall models are shown by dashed curves with the fitted parameters in the corresponding P–V diagrams (see Appendix D).

overlapped with M1, while areas 2 and 3 are located on the northern and southern sides of M1, respectively. Compared with Figures 3(a) and (b), one can see that the three areas are coincident with the velocity-increasing features in the peak velocity maps.

The similar increasing features of velocity dispersion have been interpreted as chemically fresh gas inflow (traced by the HC_3N line) around an accreting low-mass young star (see Pineda et al. 2020). In addition, the accretion flows funneling material to disk scales resembling spiral features and filaments (traced by $H^{13}CO^+$; see Sanhueza et al. 2021) detected in an HMYSO also show a large velocity dispersion toward the central star. In this sense, the features shown in Figure 3(c) could reflect the streamer being accelerated and spinning up as it enters the torus structure around the M1. To investigate the potential accretion streamers, we inspected the different molecular emissions closer to M1 and found the streamers along two directions traced by the chemically fresh molecules including HC_3N, CCH and HCO$^+$, as shown in Figures 4 and 5.

Figure 4 shows the HCO$^+$ emission region observed with ALMA and SMA. It has an overall spatial extension from M1 and M2. The HCO$^+$ emission observed with SMA is less extended than its ALMA counterpart, which is possibly due to

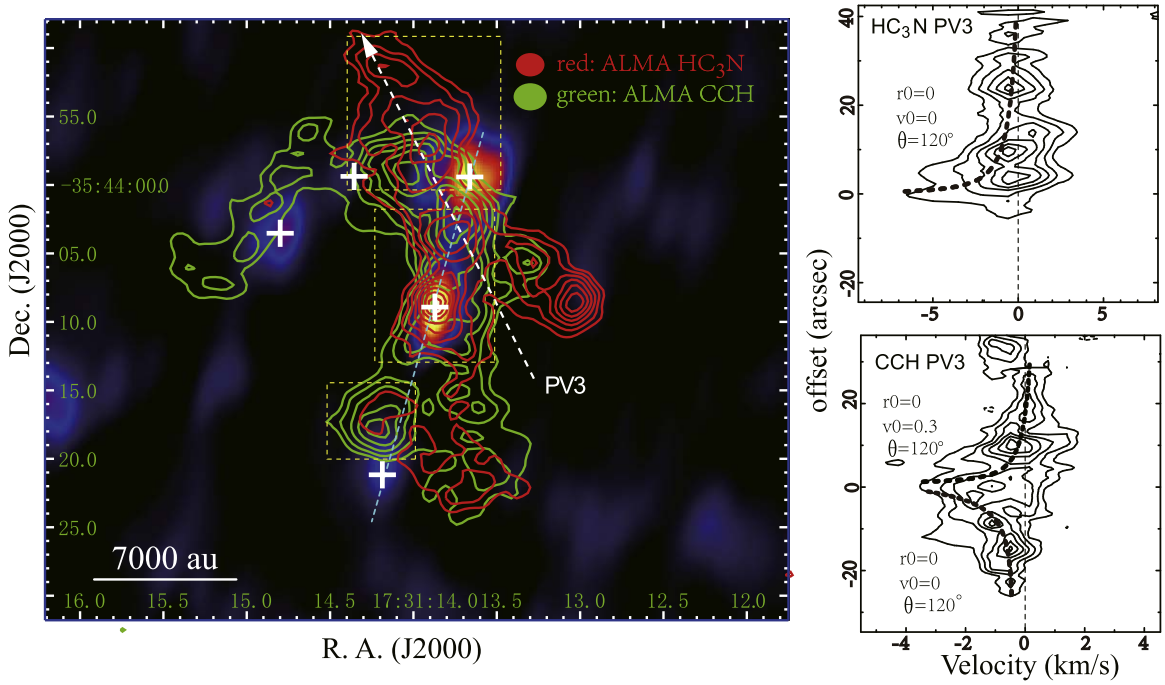

Figure 5. Same as Figure 4, but for the northwestern infalling streamer (Streamer 2) traced by the ALMA CCH and HC_3N lines. The contour levels for both CCH and HC_3N start from 0.24 Jy beam^{-1} km s^{-1} in steps of 0.08 Jy beam^{-1} km s^{-1}. The right subpanels show the P–V plot along Streamer 2 for HC_3N and CCH. The contour levels start from 30% in steps of 10% of the peak value (0.12 Jy beam^{-1} for HC_3N and 0.17 Jy beam^{-1} for CCH). The best freefall models are shown by dashed curves with the fitted parameters in the corresponding P–V diagrams (see Appendix D).

the less complete spatial coverage by the SMA baselines. But it still shows an overall consistent spatial morphology. M3 is devoid of HCO^+ (1–0) as seen in both SMA and ALMA data. This could be due to the depletion effect in cold dense gas therein. This is in accordance with the intense DCO^+ emission at M3, which also indicates the deuteration due to the cold dense environment.

The HCO^+ emission region also has an additional spatial extension from southwest to northeast over M2. We plot the P–V diagram along this gas component as shown in the right panels in Figure 4. For both the SMA and ALMA data, the gas exhibits a steep velocity increase toward the major axis (dashed arrow in Figure 4). The SMA data have a slightly different spatial shape and weaker emissions on the western side than the ALMA data, but on the eastern side, the two data sets have very coincident velocity profiles, with the bulk velocity increasing from $v - v_{\rm sys} = -1$ to -4 km s^{-1}. The velocity peak on the axis is overlapped with the increased velocity dispersion in area 2 (Figure 3(c)). The HCO^+ and CCH emissions should therefore consistently demonstrate the gas interaction around M2. The velocity increase toward M2 is different from either outflow or disk rotation. Moreover, the HCO^+ extension has a large angle ($\sim$70° to 90°) from the major axis of the torus. The velocity increase is therefore more likely to indicate an infall motion toward the torus midplane. It is denoted as infall streamer 1.

A similar velocity profile is also seen along the filament branch on the northeast, which connects M4 to the major axis, as shown in Figure 5. The P–V diagrams along this direction are shown in the right subpanels. Similar to the streamer 1, CCH also exhibits steeply increased velocity toward the major axis from both sides with a scale of -3 km s^{-1}. The P–V plot of HC_3N is shown in the upper-right subpanel in Figure 5. Despite the low velocity resolution ($v_{\rm chan} = 1.4$ km s^{-1}), the velocity-increasing trend is still evidently discernible. The two species together suggest a similar infall streamer along the PV3 direction toward the major axis, which is denoted as streamer 2.

We note that another streamer with distinct velocities is also seen along M5 to M4 (see Figures 3(a) and (b)). There is a large velocity dispersion of the CCH line around the M4 position (see Figure 3(c)). It could be speculated that this streamer is colliding with the main streamer at the M4 position and eventually enters the main streamer at this position.

Assuming the streamers are in freefall due to the gravity of a central mass, we can fit the P–V diagrams to a very consistent degree by adjusting the inclination angle of the streamer and the projection height of the landing point of the streamer onto the torus using Equation (D1) in Appendix D. As shown in Figures 4 and 5, for all the species, the velocity profiles (dashed lines in Figures 4 and 5) have landing points close to the major axis. The streamers should thus have a converging trend onto the torus. Since all the molecular species are chemically fresh, they suggest that the streamers should come from the cold dense environment around the torus. However, the landing points along the major axis (blue circles) have an offset of $\sim$3000 au from M1. This suggests that the streamers should have first reached the torus surface, and then joined the disk accretion around the central HMYSO as the second step. The spatial and kinematical structures, including the streamers, are shown in a schematic view in Figure E1. The infall motion such as this could provide a more stable mass supply than the global infall directly toward the HMYSO.

2.4. Contribution of the Infalling Streamers to Mass Growth

For the streamers, we derived their excitation temperature, column densities, masses, and infall rates following the methods in Appendix C. For Streamer 2, we estimated $T_{\rm ex} = 10$ K from CCH hyperfine components and a total mass of $\sim$2.5 $M_\odot$. Since the CCH emission is much weaker in the

southern streamer, we instead used the HCO^+ (3–2) line for the calculation. Assuming the streamer is optically thin at a similar temperature of $T_{ex} = 10$ K and typical HCO^+ abundance of $[HCO^+/H_2] = 1.2 \times 10^{-9}$ (Sanhueza et al. 2013), we derived a total gas mass of $\sim 1.5\,M_\odot$. We see that the two streamers have comparable masses.

For the streamers, we estimated a typical freefall timescale of $t_{ff} \sim 4.6 \times 10^4$ yr (see Appendix D). Using this value, we can estimate the infall rates along these streamers to be about $\dot{M}_{in,streamers} = 5.5 \times 10^{-5}\,M_\odot$ yr^{-1} for the northwestern streamer and $3.1 \times 10^{-5}\,M_\odot$ yr^{-1} for the southeastern streamer. Together they provide a total infall rate of $8.6 \times 10^{-5}\,M_\odot$ yr^{-1}. Compared to the similar streamer found in IRAS 18089–1732 (Sanhueza et al. 2021), we can see that the two systems have comparable spatial scales of $\sim 10^4$ au and infall rates of $(9–25) \times 10^{-5}\,M_\odot$ yr^{-1}. Therefore, the accretion streamers might play important roles in high-mass star formation.

Assuming that the HMYSO has a formation timescale comparable to the accreting timescale $t_{ff} = 4.6 \times 10^4$ yr, it could have an overall infall rate of $\dot{M}_{in,all} = M_*/t_{ff} \sim 2.6 \times 10^{-4}\,M_\odot$ yr^{-1} during its formation. Compared with the infall rate of the streamers, we have a ratio of $\dot{M}_{in,streamers}/\dot{M}_{in,all} = 0.33$. Considering that the freefalling state is the most extreme infall state, the streamers might contribute at least one-third of the material in the accretion process to the HMYSO. This is comparable to the values of low-mass counterparts within a factor of 2 to 3 (see details in Pineda et al. 2020). This similarity supports the hypothesis that both low- and high-mass protostars have a considerable mass supply from inflowing streamers. In G352.63, the detection in chemically fresh tracers further suggests that the streamers originate from the surrounding cold gas environment.

Besides providing a mass supply, the streamers could also impact the disk system and influence its formation and evolution. If the impact is sufficiently strong, it might cause disk fragmentation, which in turn can produce transient events such as episodic accretion bursts (e.g., Chen et al. 2020b). Other possible disk-mediated accretion bursts have also been discovered in both high-mass (Lee et al. 2021) and low-mass regions (Hartmann & Kenyon 1996; Fischer et al. 2019). All these studies have a general agreement with the theoretical model that predicts a considerable (up to half) stellar mass coming from these accretion events (Meyer et al. 2019). In the case of G352.63, the contribution of streamer accretion to the star mass growth is comparable in fraction to the above episode accretions. This supports the expectation in the model that the accretion streamers could be an additional mechanism to induce disk fragmentation besides the gravitational instability in the disk (e.g., Meyer et al. 2017, 2019). However, new numerical calculations are still required to investigate such a kinematic processes. Although at present there are no observations to show that G352.63 has accretion burst events, this source can be an excellent target for future work to explore the link between streamers and variability induced by the accretion. Furthermore, similar high-angular resolution observations in more regions are required to clarify the frequency and importance of these streamers during the high-mass star-forming process.

3. Summary

In the nearby high-mass star-forming region G352.63, we have detected clear signatures of gravitational infalling streamers toward a compact and flattened gas structure, which could resemble a dense gas torus around an HMYSO with a mass of $\sim 10 M_\odot$. The streamers should mainly consist of cold dense gas ($\sim$10 K) due to their detection in the chemically fresh molecules CCH, HC_3N, and HCO^+. The HMYSO is in a sparsely clustered environment and also associated with a set of bipolar outflows, but the other gas components can all be clearly distinguished from the infalling streamers. The infall rate of the G352.63 streamers is estimated to be $8.6 \times 10^{-5}\,M_\odot$ yr^{-1}, which contributes one-third of the accretion material fed to the HMYSO mass growth. Such a fraction is comparable to that of the infalling streamers toward low-mass YSOs. Therefore, chemically fresh infalling streamers could play a critical role in transferring cold dense gas into the accretion disk around the HMYSO as in low-mass ones.

We are grateful for the support from the operators of the ALMA and SMA during the observations. This work was supported by the National Natural Science Foundation of China (11873002, 12011530065, 11590781). X.C. is thankful for the Guangdong Province Universities and Colleges Pearl River Scholar Funded Scheme (2019). S.P.E. acknowledges the support of the ARC Discovery Project (project number DP180101061). A.M.S. work was supported by the Ministry of Education and Science of the Russian Federation within the framework of the research activities (project no. FEUZ-2020-0030).

Appendix A
Gas Temperature in the Hot Molecular Core in M1

Hot molecular core tracers (such as CH_3CN and CH_3OH) were only detected toward a compact region (not resolved by either the ALMA nor SMA observations) toward the dust component M1. We have assumed that the molecular gas is in local thermodynamic equilibrium (LTE) to estimate physical parameters. The column density can be calculated using a general formula (e.g., Blake et al. 1987; Chen et al. 2013):

$$N = \frac{3k_B W}{8\pi^3 \nu S\mu^2} \frac{T_{ex}}{T_{ex} - T_{bg}} \frac{\tau}{1 - \exp(-\tau)} \times Q(T_{ex}) \exp(E_u/k_B T_{ex}), \quad \text{(A1)}$$

where k_B is the Boltzmann constant in erg K^{-1}, W is the observed line integrated intensity of the line profile in unit of K km s^{-1}, ν is the frequency of the transition in Hz, and $S\mu^2$ is the product of the total torsion-rotational line strength and the square of the electric dipole moment, E_u/k_B is the upper-level energy in K, and $Q(T_{ex})$ is the partition function at temperature T_{ex}.

When the molecular emission is optically thin and in LTE, we can determine the rotational temperature (T_{rot}) from rotation diagram analysis. The standard formula for such analysis can be derived from Equation (A1) as follows:

$$\ln\left(\frac{3k_B W}{8\pi^3 \nu S\mu^2}\right) = \ln\frac{N(T_{rot} - T_{bg})}{Q(T_{rot})} - \frac{E_u}{k_B T_{rot}}. \quad \text{(A2)}$$

A straight line fitted to a plot of $\ln(3k_B W/8\pi^3\nu S\mu^2)$ versus E_u/k_B will have a slope of $1/T_{rot}$. We used eight transitions of CH_3CN (from $12_0 - 11_0$ to $12_7 - 11_7$ with frequencies in the range 220.5–220.8 GHz) detected in the SMA observations to estimate the rotation temperature of the hot gas in M1 (shown

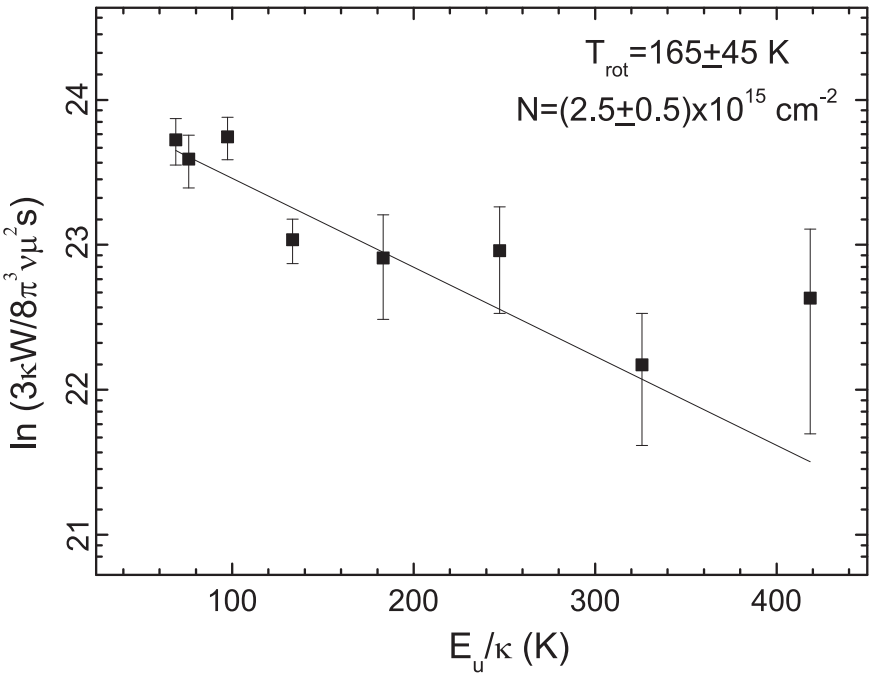

Figure A1. The CH_3CN rotation diagram of the M1 core. The solid line is the best fit to the rotation diagram and the fit results are shown in the top right.

in Figure A1). The derived gas rotation temperature is 165 ± 45 K, confirming that M1 corresponds to a hot molecular core.

Appendix B
Kepler Rotation Model for the M1–M2–M3 Disk/Torus System

In the case of a system undergoing Keplerian rotation (as shown in Figure 2), the speed of rotation along the line of sight for a given enclosed mass (M) and radius (r) along the disk/torus satisfies the following relation:

$$\frac{v(r) - v_0}{\sin\theta} = \sqrt{\frac{GM}{r - r_0}}, \tag{B1}$$

where G is the gravitational constant, v_0 is the systemic velocity of the disk/torus system, θ is the inclination angle of the disk/torus rotational axis, and r_0 is the reference offset on the P–V diagram (i.e., the central star position in M1). By adjusting the parameters M, v_0, and r_0 to fit the P–V diagrams of the disk tracers H_2CO and DCN, we find $M = 9.0/\sin^2\theta\, M_\odot$, $v_0 = -0.3$ km s^{-1} and $r_0 = -1000$ au (or $-1\farcs5$) provide the best fit to the data. Furthermore, if we assume an inclination angle of $\theta = \sim 60°$, as based on the distorted structures traced by DCO^+ and dust emission at M3, we then estimate an enclosed mass of $\sim 12\, M_\odot$ in this rotational system. We note that due to the nonzero r_0, the gravitational center of the rotational system is not exactly at the continuum emission peak of M1, but at a position of 1000 au northward along the P–V slice (see Figure 2). This may be caused by inhomogeneous material distribution in the disk/torus system.

Appendix C
Cold Gas Properties of the Infalling Streamers

Under LTE conditions, we assume an excitation temperature (T_{ex}) equal to the gas kinematic temperature. CCH is one of the chemically fresh molecules in the streamers. It has two major hyperfine components (HFCs), including NJF = 1(3/2)2 − 0 (1/2)1 and 1(3/2)1 − 0(1/2)0. We used their intensity ratio to derive the excitation temperature. First, the optical depth of the main component $F = 2 - 1$ can be estimated using the following relation:

$$\frac{T_{B,s}}{T_{B,m}} = \frac{1 - \exp(-0.5\tau_m)}{1 - \exp(-\tau_m)}, \tag{C1}$$

where $T_{B,m}$ and $T_{B,s}$ are the observed brightness temperature in K for the main and satellite components, respectively. We have determined that the expected opacity ratio (R) between the main and satellite lines is $\tau_m/\tau_s = 2$, under optically thin conditions. We can further calculate the excitation temperature using the relation:

$$T_B = T_0\left(\frac{1}{e^{T_0/T_{ex}} - 1} - \frac{1}{e^{T_0/T_{bg}} - 1}\right)(1 - e^{-\tau}), \tag{C2}$$

where T_{bg} (=2.73 K) is the background brightness temperature and $T_0 = h\nu/k_B$.

We obtain the ratio between the peak intensities of the CCH maps of the two hyperfine transitions (from ALMA observations) to estimate the optical depth and excitation temperature in each pixel. The derived excitation temperature distributions are illustrated in Figure C1. The excitation temperatures are in the range of 8–20 K, with a typical value of ∼10 K. The streamers can almost be traced by the CCH (in particular for the northern one), indicating that the streamers are chemically fresh and in a cold environment.

The molecular column density can also be derived from its intensity using Equation (A1). The total column density $N_{tot}(H\,I + H_2)$ is then derived from N_{mol} and the chemical abundance of $X_{mol} = N_{mol}/N_{tot}$. For CCH, we assumed a typical CCH abundance of $X(CCH) = 8 \times 10^{-9}$ (Ginard et al. 2012).

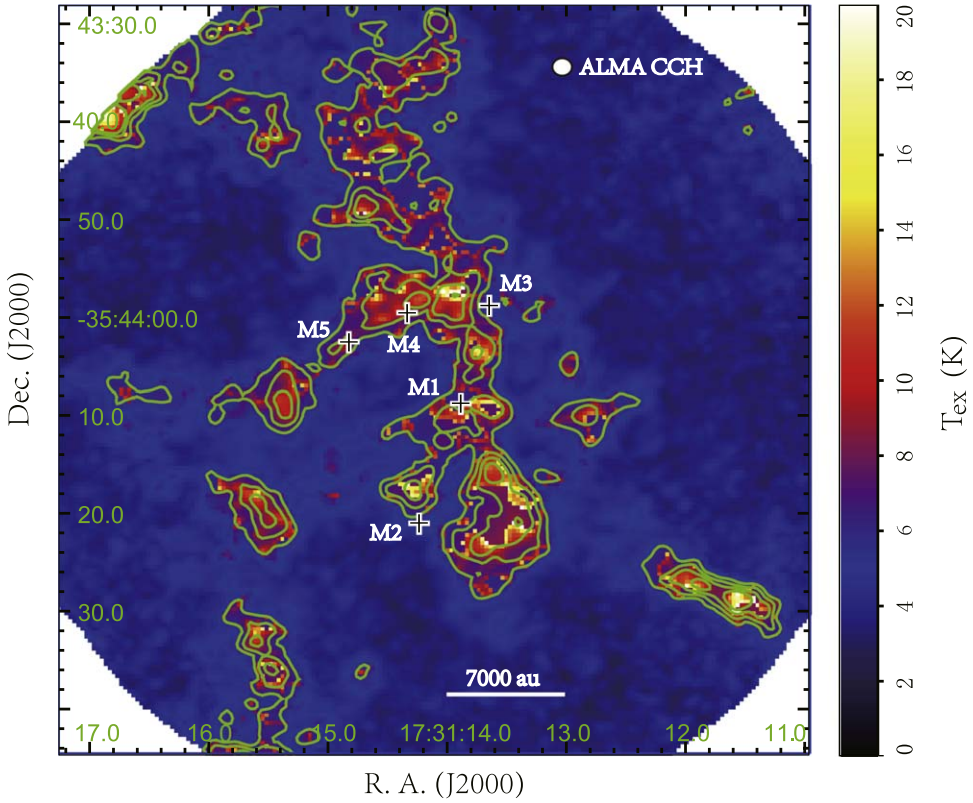

Figure C1. The excitation temperatures of the CCH derived from its two hyperfine lines. The background is the derived excitation temperature of the CCH. Green contours show peak flux densities of the CCH $N = 1 - 0$, $J = 3/2 - 1/2$, $F = 2 - 1$ transition, with contour levels the same as that given in the upper panel of Figure 3(b). The beam shape of the ALMA observation is given by the ellipse.

And the total mass of a gas clump is

$$M_{\rm c} = \int \mu m_{\rm H} N_{\rm tot}\, {\rm dA}, \tag{C3}$$

wherein $\mu = 2.33$ is the mean molecular weight (Myers & Benson 1983).

Appendix D
Gravitationally Controlled Infalling Streamers

In the case of gravitationally controlled infall, it is possible to estimate the speed of freefall for an enclosed mass (M) and radius (r) using the relation:

$$\frac{v(r) - v_0}{\cos\theta} = \sqrt{\frac{2GM}{r - r_0}}, \tag{D1}$$

where θ is the inclination angle of the streamer along the line of sight, v_0 is the velocity at the starting position of the streamer, and R_0 is the projection height of the landing point of the streamer onto the disk/torus. We have assumed $M \sim 12 M_\odot$, the mass derived from the rotational disk/torus system and adjusted the parameters θ, v_0, and R_0 to fit the P–V distributions of the infalling streamers shown in Figures 4 and 5. These P–V diagrams can be well fit using this method, suggesting that the streamers are moving toward the disk/torus under gravitational attraction. The values estimated for θ, v_0, and R_0 are different for each streamer, indicating that the infalling directions of these streamers and the landing point on the disk/torus are different.

The freefall timescale of the infalling streamers can be derived as

$$t_{ff} = \sqrt{\frac{r^3}{GM}}. \tag{D2}$$

For these streamers, the typical observed length R in the sky plane is equal to $\sim 1.0 \times 10^4$ au, and for $M = 12\, M_\odot$, the freefall timescale is $\sim 4.6 \times 10^4$ yr.

Appendix E
A Carton for the Spatial and Kinematical Structures

The ALMA and SMA observations made the detections of the complicated nature toward our target system, with multiple dense cores, several streamers with different tracers, the torus, and the outflows. For clarifying these spatial and kinematic structures of this system, a simple cartoon is drawn to summarize all of these components in Figure E1.

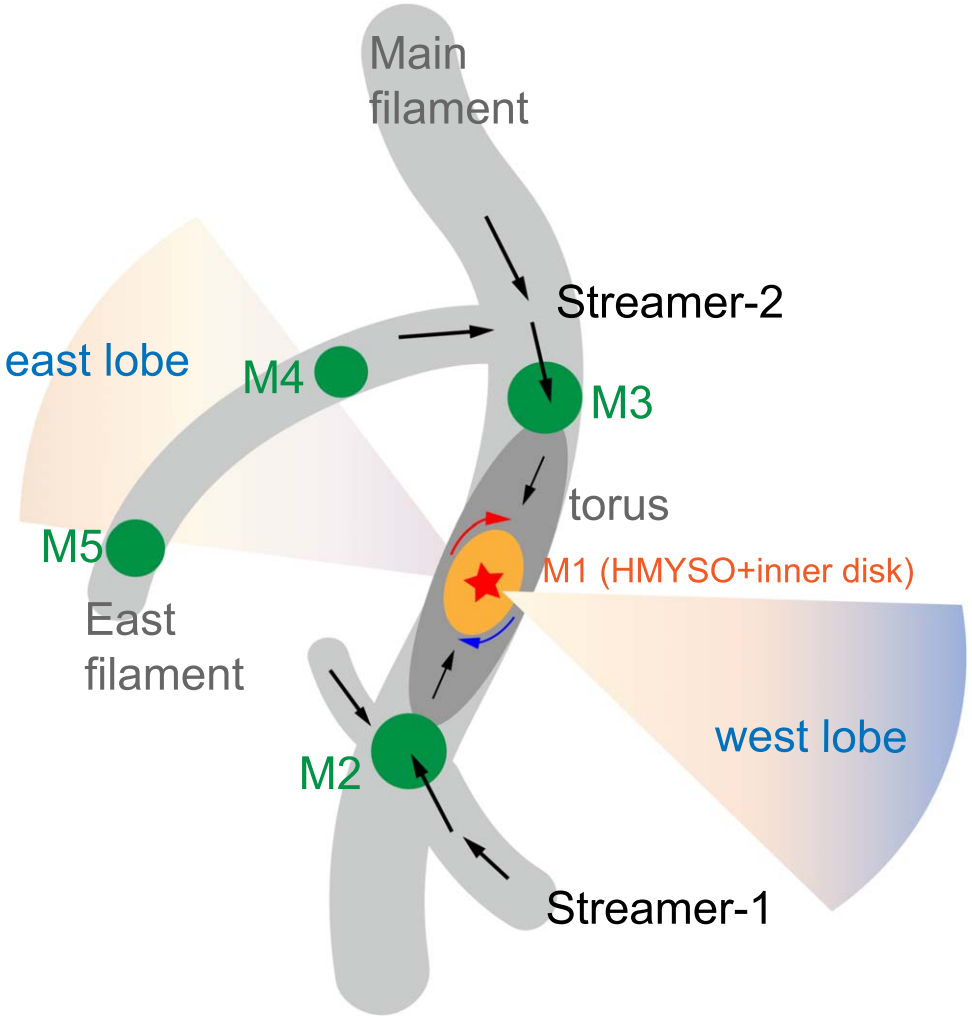

Figure E1. A schematic view for the dense gas structure and kinematic features in G352.63.

ORCID iDs

Xi Chen https://orcid.org/0000-0002-5435-925X
Tie Liu https://orcid.org/0000-0002-5286-2564
Ke Wang https://orcid.org/0000-0002-7237-3856
Zhi-Qiang Shen https://orcid.org/0000-0003-3540-8746
Simon P. Ellingsen https://orcid.org/0000-0002-1363-5457
Ying Mei https://orcid.org/0000-0002-7960-9251
Yue-Fang Wu https://orcid.org/0000-0002-5076-7520
Kee-Tae Kim https://orcid.org/0000-0003-2412-7092

References

Avison, A., Fuller, G. A., Peretto, N., et al. 2021, A&A, 645, A142
Beltrán, M. T., Sánchez-Monge, Á., Cesaroni, R., et al. 2014, A&A, 571, A52
Bergin, E. A., & Tafalla, M. 2007, ARA&A, 45, 339
Blake, G. A., Sutton, E. C., Masson, C. R., et al. 1987, ApJ, 315, 621
Bonnell, I. A., & Bate, M. R. 2006, MNRAS, 370, 488
Bonnell, I. A., Vine, S. G., & Bate, M. R. 2004, MNRAS, 349, 735
Cesaroni, R., Massi, F., Arcidiacono, C., et al. 2013, A&A, 549, A146
Chen, H.-R. V., Zhang, Q., Wright, M. C. H., et al. 2019a, ApJ, 875, 24
Chen, M. C.-Y., Di Francesco, J., Rosolowsky, E., et al. 2020a, ApJ, 891, 84
Chen, X., Gan, C.-G., Ellingsen, S. P., et al. 2013, ApJS, 206, 9
Chen, X., Li, J.-J., Zhang, B., et al. 2019b, ApJ, 871, 198
Chen, X., Sobolev, A. M., Ren, Z.-Y., et al. 2020b, NatAs, 4, 1170
Fischer, W. J., Safron, E., & Megeath, S. T. 2019, ApJ, 872, 183
Ginard, D., González-García, M., Fuente, A., et al. 2012, A&A, 543, A27
Goddi, C., Ginsburg, A., Maud, L. T., et al. 2020, ApJ, 905, 25
Hacar, A., Tafalla, M., Forbrich, J., et al. 2018, A&A, 610, A77
Hartmann, L., & Kenyon, S. J. 1996, ARAA, 34, 207
Hu, B., Qiu, K., Cao, Y., et al. 2021, ApJ, 908, 70
Ilee, J. D., Cyganowski, C. J., Nazari, P., et al. 2016, MNRAS, 462, 4386
Johnston, K. G., Robitaille, T. P., Beuther, H., et al. 2015, ApJL, 813, L19
Kuffmeier, M., Calcutt, H., & Kristensen, L. E. 2019, A&A, 628, A112
Kuznetsova, A., Hartmann, L., & Heitsch, F. 2019, ApJ, 876, 33
Lee, Y.-H., Johnstone, D., Lee, J.-E., et al. 2021, ApJ, 920, L119
Liu, T., Evans, N. J., Kim, K.-T., et al. 2020, MNRAS, 496, 2790
Maud, L. T., Cesaroni, R., Kumar, M. S. N., et al. 2018, A&A, 620, A31
Maud, L. T., Cesaroni, R., Kumar, M. S. N., et al. 2019, A&A, 627, L6
McKee, C. F., & Tan, J. C. 2002, Natur, 416, 59
McKee, C. F., & Tan, J. C. 2003, ApJ, 585, 850
Meyer, D. M.-A., Vorobyov, E. I., Elbakyan, V.-G., et al. 2019, MNRAS, 482, 5459
Meyer, D. M.-A., Vorobyov, E. I., Kuiper, R., & Kely, W. 2017, MNRAS, 464, L90
Murillo, N. M., van Dishoeck, E. F., Hacar, A., Harsono, D., & Jørgensen, J. K. 2021, arXiv:2111.04039
Myers, P. C., & Benson, P. J. 1983, ApJ, 266, 309
Öberg, K. I., Furuya, K., Loomis, R., et al. 2015, ApJ, 810, 112
Peretto, N., Fuller, G. A., Duarte-Cabral, A., et al. 2013, A&A, 555, A112
Pety, J., Goicoechea, J. R., Hily-Blant, P., et al. 2007, A&A, 464, L41
Pineda, J. E., Segura-Cox, D., Caselli, P., et al. 2020, NatAs, 4, 1158
Ren, Z., Zhu, L., Shi, H., et al. 2021, MNRAS, 505, 5183
Sanhueza, P., Girart, J. M., Padovani, M., et al. 2021, ApJL, 915, L10
Sanhueza, P., Jackson, J. M., Foster, J. B., et al. 2013, ApJ, 773, 123

Shu, F. H., Adams, F. C., & Lizano, S. 1987, ARA&A, 25, 23
Tackenberg, J., Beuther, H., Henning, T., et al. 2014, A&A, 565, A101
Tan, J. C., Beltrán, M. T., Caselli, P., et al. 2014, in Protostars and Planets VI, ed. T. K. Henning et al. (Tucson, AZ: Univ. Arizona Press), 149
Thieme, T. J., Lai, S.-P., Lin, S.-J., et al. 2021, arXiv:2111.04001
Tobin, John J., Looney, L. W., Li, Z.-Y., et al. 2016, ApJ, 818, 73
Wurster, J., Bate, M. R., & Price, D. J. 2019, MNRAS, 489, 1719
Xu, Y., Li, J. J., Hachisuka, K., et al. 2008, A&A, 485, 729
Yuan, J., Li, J. Z., & Wu, Y. 2018, in IAU Symp. 336, Astrophysical Masers: Unlocking the Mysteries of the Universe, ed. A. Tarchi, M. J. Reid, & P. Castangia (Cambridge: Cambridge Univ. Press), 299
Yuan, L., Li, G.-X., Zhu, M., et al. 2020, A&A, 637, A67
Zapata, L. A., Garay, G., Palau, A., et al. 2019, ApJ, 872, 176
Zemlyanukha, P. M., Zinchenko, I. I., Salii, S. V., et al. 2018, ARep, 62, 326
Zinchenko, I. I., Liu, S.-Y., Su, Y.-N., et al. 2020, ApJ, 889, 43
Zinnecker, H., & Yorke, H. W. 2007, ARA&A, 45, 481